Journal of Power Sources 552 (2022) 232217

Contents lists available at ScienceDirect

Journal of Power Sources

journal homepage: www.elsevier.com/locate/jpowsour

Computational assessment of the thermal response of a Li-ion battery module to transient loads

Ali Saeed [a], Nader Karimi [a,b,*], Manosh C. Paul [a]

[a] James Watt School of Engineering, University of Glasgow, Glasgow, G12 8QQ, United Kingdom
[b] School of Engineering and Materials Science, Queen Mary University of London, London, E1 4NS, United Kingdom

HIGHLIGHTS

- A novel measure of battery heat release due to internal heat generation is presented.
- Transient cases with sharp gradients cause large delays in system response.
- Air cases always produce an overshoot and are far slower at reaching steady state.
- Battery cells remain within the safe operating range in almost all water cases.
- Water cases react far quicker to changes in the internal heat generation.

ARTICLE INFO

Keywords:
Battery thermal management
Temperature control
Transient response
Electric vehicle

ABSTRACT

This paper provides a methodology to assess the average surface temperature of battery cells under realistic transient scenarios. Computational fluid dynamics modelling of battery cooling is conducted for the cases exposed to the ramps of internal heat generation inferred from the standard driving cycles. The results are then post-processed to determine the effectiveness of air and water as the coolant fluids. A quantitative measure of the maximum overshoot, dimensionless settling (DST), heating (DHT), and cooling (DCT) time is subsequently presented. It is shown that, compared to water, air produces a considerably delayed response to temporal changes in the internal heat generation and is slower at reaching the new steady state condition. Cooling battery cells by using water almost always ensures remaining within the safe operating range. Nonetheless, regardless of the coolant type, the long period ramps tend to produce smaller values of DST. The primary origin of the delay is the slow heat conduction within the battery cells. In addition, it is shown that water responds to changes in the internal heat generation far quicker during the heating and the cooling phases. The study highlights the importance of transient analyses for characterising the thermal behaviour of battery packs.

1. Introduction

Electric Vehicles (EVs) have gained vast attention due to significant efforts being made worldwide to combat the rising environmental concerns and reduce greenhouse gas emissions [1,2]. Improvements in energy storage technologies have significantly increased the battery-powered vehicle trend. However, EVs still face the major challenge of finding an energy source capable of high performance, high mileage, and fast charging [3,4]. Lithium-ion (Li-ion) batteries have gained considerable deliberation for use within EVs due to their lightweight, high energy density, prolonged life, and recyclability [5] as compared to their lead or nickel-metal based counterparts [6]. Nevertheless, the battery's safety, lifetime, and discharge capacity greatly depend on the operational temperature. Consequently, battery temperature control has become crucial to EVs' management systems.

Former studies [7,8] have indicated that to sustain an electrochemical rate of reaction for a healthy and safe operation, the battery cell temperature should be between 25 °C and 45 °C. Excessively high or low temperatures may lead to electrolyte decomposition causing irreversible electrolyte loss and decreasing battery capacity [9,10]. Further, the cell to cell temperature variation should not exceed 5 °C [11]. Developing such hot spots within a battery module can alter the battery's charging and discharging capabilities, resulting in irreversible damage and a shortened lifetime [12,13]. The long-term presence of uneven temperature distribution across the battery cells can cause poor

* Corresponding author. James Watt School of Engineering, University of Glasgow, Glasgow, G12 8QQ, United Kingdom.
E-mail address: n.karimi@qmul.ac.uk (N. Karimi).

https://doi.org/10.1016/j.jpowsour.2022.232217
Received 12 July 2022; Received in revised form 27 September 2022; Accepted 4 October 2022
Available online 21 October 2022

Abbreviation

a	Acceleration (m/s^2)
α	Thermal diffusivity (m^2/s)
c_p	Specific heat capacity (J/kg·K)
D	Diameter (m)
H	Height (m)
h	Heat Transfer Coefficient (W/m^2·K)
I	Battery cell current draw (A)
k	Thermal Conductivity (W/m·K)
L	Single Cell Section Length (m)
m	Mass (kg)
Nu	Nusselt Number (−)
P	Pressure (Pa)
Re	Reynolds Number (−)
R_I	Internal battery cell resistance (Ω)
R	Radius (m)
S_c	Volumetric cell source term (W/m^3)
T	Temperature (K)
q''	Heat flux (W/m^2)
u	Velocity (m/s)
$\overline{u}$	Average Velocity (m/s)
v	Cell volume (m^3)
x, y, z	Cartesian Coordinate System

Greek Symbols

ρ	Density (kg/m^3)
$\overline{\rho}$	Average Density (kg/m^3)
μ	Dynamic Viscosity (kg/m·s)
τ	Shear Stress (Pa)
δ	Kronecker Delta Function

Subscripts

i, j, k	Coordinate Directions
f	Fluid
s	Solid

uniformity within a battery pack, leading to each battery cell displaying a variety of thermal effects, amplifying the temperature variations and developing a vicious cycle [14–16]. Numerous battery thermal management systems (BTMS) have been considered to combat excessive temperatures and maximise the battery cell lifetime, from forced air and water cooling to phase change materials for passive cooling, see Refs. [17–19]. Designing such systems requires further depth into the internal heat generation, thermal transport, and heat dissipation mechanisms. Most importantly, the highly complex and dynamic heat generation in Li-ion batteries, time-dependent thermal management systems are crucial [17,18,20]. However, only a few studies have focused on the heat transfer of Li-ion cells under transient loads [17,21,22], while most of those studies are primarily concerned with the methods of heat generation inside battery cells [23,24]. In the followings, a review of the existing studies on the thermal management of Li-ion batteries under dynamic loads is put forward.

Huang et al. [25] investigated the battery module's transient and ultimate thermal behaviours using a liquid coolant. These authors used a lumped mass model with a central cold plate cooling design to simulate a battery thermal management system. Their study focused on understanding the relationship between discharge rate, inlet flow rate, and the heat transfer coefficient. They concluded that increasing the inlet flow rate of water will result in the battery module being cooled more effectively but not efficiently, resulting in an upper limit to the effectiveness of the inlet flow rate. Further, an abrupt change in the inlet flow would cause the cooling system's response time to experience a hysteresis effect. Huang et al. also presented two empirical correlations, one for the Nusselt number and another for the time delay. Fang et al. [26] investigated the transient thermal performance of a mini-channel cold plate under sharply increasing heat loads. This study focused on the effects of the coolant flow rate, increase in heat flux and channel number. Increasing the coolant flow rate decreased the final average temperature of the battery module and the temperature deviation, as expected. However, like the study of Huang et al. [25], an upper limit of the coolant flow rate was also found here, where exceeding this limit hurts the effectiveness of the BTMS. It was observed that increasing the heat flux of the battery module causes an immediate increase in the average temperature and temperature deviation. Further, it was shown that increasing the channel numbers could offer a slight advantage on the average temperature. However, it could lead to worse temperature uniformity due to a negative impact on the velocity magnitude in each channel.

Saeed et al. [27] studied the dynamics of Li-ion battery cooling system to harmonic loads and for different coolants under a turbulent flow regime. They used Fast Fourier Transforms to determine the non-linearity of this thermal system. Their work showed that the battery thermal management system could be approximated as a linear dynamical system if the load disturbances were of short duration and low amplitudes. Long duration temporal disturbances of the battery surface heat flux generate a strong nonlinear response. Further, for cases which can be approximated as linear, the transfer function of Nu acts like a low-pass filter. Zhang et al. [15] presented an efficient transient heat transfer model to evaluate the temperature distribution in parallel air-cooled BTMS. In this CFD study, the authors used the k-epsilon turbulence model. They concluded that the developed transient heat transfer model could be used effectively to calculate the battery cell temperature and evaluate the performance of the different air-cooled BTMSs. Further, this study suggested optimisation techniques to enhance the cooling performance and consume less power under various flow rates. Zhu et al. [28] developed a two-phase physical model of BTMS and studied the transient thermal performance using flow rate, heat flux, and cold-source temperature. This study found that decreasing the flow rate improved the start-up time and lowered the average temperature and the maximum temperature difference while enhancing thermal performance by 25%. However, increasing the heat flux weakened the transient performance of the two-phase system by significantly increasing the start-up time and the maximum temperature difference.

Currently, existing studies on unsteady battery thermal performance are primarily concerned with the thermal performance of the battery cells under varying flow rates. Further, most studies effectively neglected the transient nature of the battery cells. Therefore, there is currently a gap in understanding thermal transient response of Li-ion battery modules due to power discharge in a short period. Therefore, the current investigation aims to address this issue by analysing the transient thermal response of a battery module due to temporal changes in the internal heat generation. The rest of the paper is structured as follows. Firstly, the numerical and theoretical methods used in the study and validation are discussed in section 2. The results are shown and discussed in section 3, and a summary of the key findings is presented in section 4.

2. Numerical and theoretical methods

2.1. Problem configuration and assumptions

Fig. 1 shows a general sketch of a battery module, the simulation model, and schematics of a single cell section. The battery module has been arranged in a staggered cell configuration with six primary cells

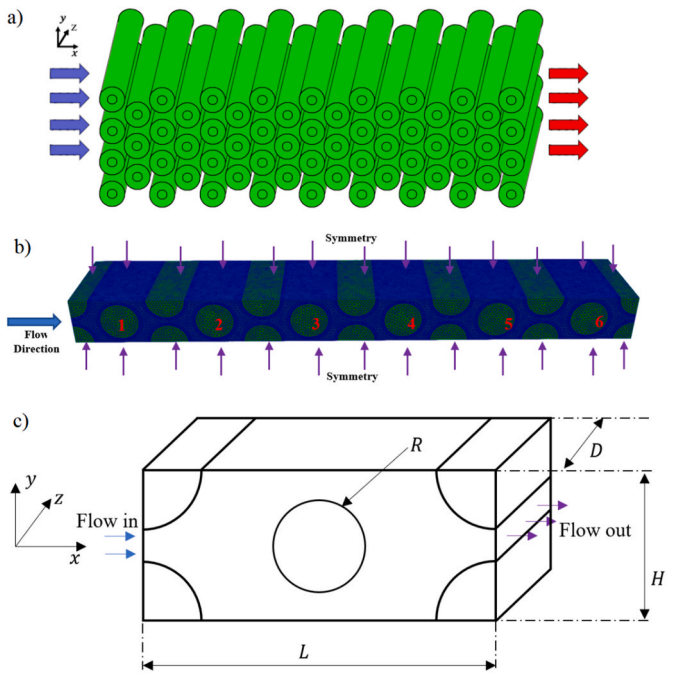

Fig. 1. a) General battery module design, b) Simulation model and c) Schematics of a single cell section.

[21,23,29]. A single cell section has a length of 100 mm [30], height of 50 mm [30], and a depth of 100 mm [30,31], as shown in Fig. 1c, and each battery cell has a radius of 20 mm [17,23,30]. The subsequent assumptions were made across the following study.

- The fluid flow inside the battery module was fully turbulent with a steady inlet velocity.
- The ideal gas model is used for air, whereas, for water, a constant density model is employed.
- Gravitational effects were neglected.

The unsteady internal heat generation was applied to each battery cell once the model reached steady-state conditions. It should be noted that when an EV is being used, the current withdrawal from battery cells causes heat generation inside each battery cell. This heat would then travel to the surface of the battery cells before being removed. Therefore, the heat generation inside each battery was modelled using a volumetric heat source, S_c, [32–34]. The relationship between this volumetric heat source and the current withdrawal from the battery cells is explained in further detail in section 2.3.

2.2. Governing equations, boundary conditions and numerical model

The flow field is modelled using the Reynolds-Averaged Navier Stokes (RANS) equations with the Boussinesq assumptions. Thus, the continuity equation is

$$\frac{\partial \rho}{\partial t}+\frac{\partial}{\partial x_j}\left(\rho\,\overline{u_j}\right)=0 \tag{1}$$

The Conservation of momentum in the x, y and z direction of the flow field are expressed by

$$\frac{\partial}{\partial t}\left(\rho\,\overline{u_i}\right)+\frac{\partial}{\partial x_j}\left(\rho\,\overline{u_i}\,\overline{u_j}\right)=-\frac{\partial \overline{P}}{\partial x_i}+\frac{\partial}{\partial x_j}\left(\overline{\tau_{ij}}-\rho\,\overline{u_i' u_j'}\right) \tag{2a}$$

$$\overline{\tau_{ij}}=\mu\left(\frac{\partial \overline{u_i}}{\partial x_j}+\frac{\partial \overline{u_j}}{\partial x_i}\right)-\frac{2}{3}\mu\left(\frac{\partial \overline{u_k}}{\partial x_k}\right)\delta_{ij} \tag{2b}$$

where, δ_{ij}, is the Kronecker delta function defined by

$$\delta_{ij}=\begin{Bmatrix}1 & i=j\\ 0 & i\neq j\end{Bmatrix} \tag{3}$$

The conservation of energy for the fluid flow is expressed as

$$\frac{\partial}{\partial t}\left(\rho c_p \overline{T_f}\right)+\frac{\partial}{\partial x_j}\left(\rho c_p \overline{u_j}\,\overline{T_f}\right)=-\frac{\partial}{\partial x_j}\left(\overline{q_f''}+\rho c_p \overline{u_j' T_f'}\right) \tag{4a}$$

$$\overline{q_j''}=\rho c_p\left(-\alpha\frac{\partial \overline{T_f}}{\partial x_j}+\overline{u_j' T_f'}\right) \tag{4b}$$

whereas the conduction of heat throughout the battery cells is defined by the Fourier's law of heat equation with an energy source term, S_c, where the definition of S_c is provided later in the text.

$$k_s\frac{\partial^2 T_s}{\partial x_i^2}+S_c=\rho_s c_{p,s}\frac{\partial T_s}{\partial t} \tag{5}$$

A symmetry boundary condition is applied to the model's top, bottom, front, and back walls since the battery pack can be expanded in both y and z-directions. The external surface of the battery cell walls is subject to a no-slip boundary condition. Further, at the interface between the battery cells, *s*, and the fluid, *f*, the temperature for both is set to be the same, $T_s = T_f$, and the heat flux entering the fluid domain is equal to the heat flux leaving the battery cells, $q_f'' = -q_s''$. Finally, the fluid inlet temperature is set to 300 K with an atmospheric outlet pressure.

The Reynolds number based on the battery cell diameter is defined as

$$\boldsymbol{Re}=\frac{\boldsymbol{u\rho D}}{\boldsymbol{\mu}} \tag{6}$$

Newtons's law of cooling is used to express the Nusselt number.

$$\boldsymbol{q''}=\boldsymbol{h}\left(\boldsymbol{T_f}-\boldsymbol{T_s}\right) \tag{7a}$$

$$\boldsymbol{Nu}=\frac{\boldsymbol{q''D}}{\boldsymbol{k_f}\left(\boldsymbol{T_f}-\boldsymbol{T_s}\right)} \tag{7b}$$

Under steady conditions, the internal heat generation within each battery cell was modelled using a constant value of 2000 W/m^3. This value was chosen to simulate a running vehicle's battery and fluid temperatures prior to introducing a large acceleration. Furthermore, the internal heat generation value was calculated based on the investigative geometry (see Fig. 1), an average energy conversion efficiency of 85% [35] and the 85 kW T Model S battery specifications [36]. Due to the air's poor thermal capacity and conductivity, high fluid velocities are required for optimal operation [37] and avoiding any damage to the battery cells. Therefore, the inlet velocity for air was chosen to be 17.5 m/s (Re = 44,000) [37]. Furthermore, a Reynolds number of 2300 was chosen for water based on other studies [38–40]. These Reynolds numbers were kept constant throughout the study. The numerical simulations were conducted using OpenFOAM v2006, an open-source, finite-volume based computational fluid dynamics software. A conjugate heat-transfer model called chtMulti Region Foam was used to simulate conduction within each battery cell due to internal heat generation and the heat transfer by the coolant flow. The latter was modelled using a three-dimensional, unsteady, turbulent flow solvers coupled with the energy equation and together with a k-ε turbulence model. Due to the difference between the two coolant fluids, different fluid models were chosen –an ideal gas model was selected for air, whereas, for water, a constant density model was utilised. The time-step was set to be five orders of magnitude smaller than the full-time scale to properly model vortex shedding [41]. Furthermore, all of the stated models use a second-order discretisation scheme for enhanced accuracy. The study was conducted on an HPC using Intel Xeon E5-2695 Broadwell series processor with 36-cores prior to being exported to MATLAB 2022a for post-processing.

2.3. Drive cycles and internal heat generation

Internal combustion vehicles emit a range of atmospheric pollutants that are all regulated using various methods around the world. However, exhaust emissions are inherently variable. Therefore, the best method to ensure repeatable test procedures is to perform all experiments under standardised laboratory conditions known as standard dynamometer drive cycles [42]. Three drive cycles were used in the present study to represent different methods of driving passenger vehicles, as shown in Fig. 2. The first cycle was the New York City (NYC) cycle, which features low-speed stop-and-go traffic conditions to represent inner-city driving. The second cycle was the SC03 drive cycle, also known as the Supplemental Federal Test Procedure (FTP) driving schedule. The final drive cycle was the Urban Dynamometer Driving Schedule (UDDS), also known as the city test. The United States Environmental Protection Agency uses these drive cycles as part of their vehicle and fuel emissions testing kit.

Furthermore, these drive cycles could be used to approximate under which condition the batteries in an electric vehicle would be under high loads. For example, an electric vehicle's battery pack would be under high load each time the car is required to accelerate to a high target speed in a very short period. Therefore, two conditions are chosen from the NYC cycle (NYCC1, NYCC2), one from the SC03 and two from the UDDS cycle (UDDS1, UDDS2), as shown in red in Fig. 2. Further, single cycle segments were also selected for analysing the thermal response of the battery module, as shown using dashed-green lines in Fig. 2.

The target speeds shown in Fig. 2 were also used to approximate the mechanical power required for each acceleration using Newton's second law of motion, described by Eq. (8). This can be converted into an equation for mechanical power by multiplying it by the change in velocity.

$$\boldsymbol{F} = \boldsymbol{ma} \tag{8a}$$

$$\boldsymbol{F} \bullet \boldsymbol{du} = \boldsymbol{ma} \bullet \boldsymbol{du} \tag{8b}$$

where the left-hand side of Eq. (8b) is the mechanical power of the vehicle. Integrating both sides of Eq. (8b) leads to the following equation describing mechanical power using mass, acceleration and velocity.

$$\boldsymbol{P} = \boldsymbol{ma}\Delta\boldsymbol{u} \tag{9}$$

P is the mechanical power, m is the mass of a Tesla Model S – 2250 kg, a is the acceleration calculated using the data given in Fig. 2, and Δu is the change in velocity, also given in Fig. 2. The battery standard used by Tesla for the Model S is based on the specifications of the 18650 lithium-ion cell format [36], the most commonly studied lithium-ion cell [43–46]. Using the mechanical power and the 18650 cell specifications, which have a voltage of 3.5 V, the battery cell current draw, I, can be calculated.

$$\boldsymbol{I} = \frac{\boldsymbol{P}}{\boldsymbol{V}} \tag{10}$$

Further, it was found that the internal resistance of a lithium-ion cell is inherently variable depending on its usage, life cycle, manufacturing quality, storage and operating temperature [44,47,48]. Therefore, the internal resistance of a battery can vary drastically, from 2.83 mΩ [44] to 81.6 mΩ [49] and as high as 140 mΩ [50] and 190 mΩ [51]. The highest internal resistance of 190 mΩ was chosen for this study as the worst-case scenario. Using the internal resistance of 190 mΩ, the current model cell geometry (see Fig. 1) and an energy conversion efficiency of 85% [35], linear ramps of volumetric internal heat generation, S_c, were calculated to represent the red and dashed-green lines shown in Fig. 2.

$$\boldsymbol{S_c} = \frac{\boldsymbol{I^2 R_I}}{\boldsymbol{v}} \tag{11}$$

where I is the battery cell current draw, R_I is the internal resistance of the battery cell and v is the cell volume.

2.4. Grid independency and validation

An unstructured tetrahedral mesh for both fluid and the solid domains was produced. The fluid domain also had prism cells for proper capturing of the boundary layer (see Fig. 1b). This type of mesh was chosen to reduce the skewness of each cell and minimise the overall cell count. A total of eight tests were carried out with varying cell sizes to determine the grid at which the highest accuracy could be achieved, while minimising computational burden. Once each battery cell's Nusselt number (Nu) falls within a variation band of 1%, the grid independency was deemed completed. These tests were computed at an Re of 4000. The results of the grid independency are shown in Table 1. As the cell size decreases, the mesh density increases, and the solution converges to within an error margin of 1%. The model accuracy and

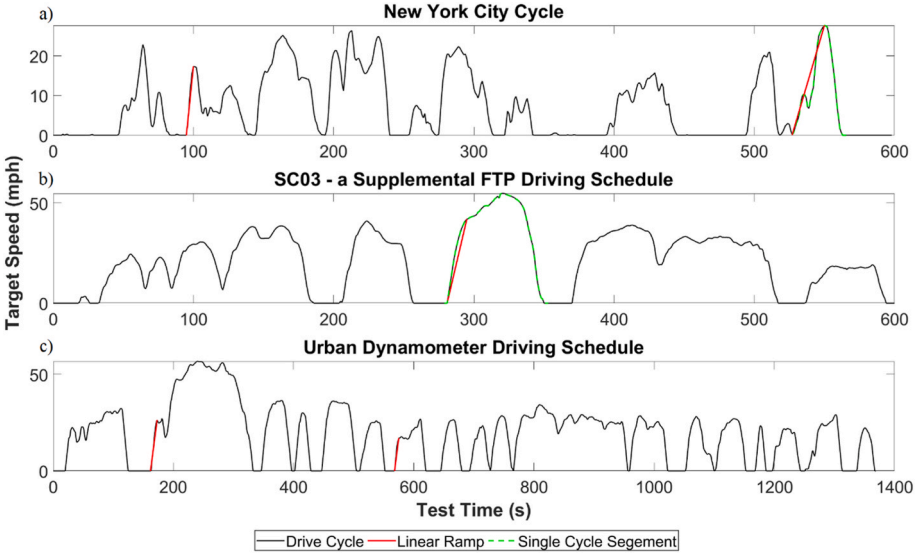

Fig. 2. Standard drive cycles. a) New York City cycle, b) SC03 drive cycle and c) Urban Dynamometer Driving cycle, where the solid-red lines represent the linear ramps and the dashed-green lines were used for the single segment. (For interpretation of the references to colour in this figure legend, the reader is referred to the Web version of this article.)

Table 1
Grid independency tests.

	Cell size (m)	Number of cells	Maximum change in *Nu* (%)
Test 1	0.008	150,517	–
Test 2	0.006	171,952	5.12
Test 3	0.005	259,783	7.01
Test 4	0.004	457,927	4.28
Test 5	0.003	973,331	3.21
Test 6	0.002	2,830,531	1.13
Test 7	0.0015	5,978,251	0.62
Test 8	0.001	16,754,751	0.10

computational demand is further balanced by selecting a cell size of 0.00175.

The present study was validated by assessing against existing experimental and numerical data. These comparisons can be seen in Fig. 3. Firstly, the model parameters are modified, so the flow occurs over a single-cylinder rather than a bundle of cylinders. A comparison of the single-cylinder air model against the Churchill and Bernstein [52] and the Hilpert [53] empirical correlation is shown in Fig. 3a. The simulated results are in exceptional agreement with the two previously stated correlations at low values of Re. As Re is increased, the error also increases, with the max error being 6.96% at a Reynolds number of 10, 000. However, it should be noted that this is still inside the expected error limits since the empirical correlations themselves can have errors as high as 20% [52].

To evaluate the unsteady performance of the solver, the current configuration without any battery cells was exposed to ramped disturbances in the flow temperature. To verify the unsteady characteristics of the simulation, the corresponding changes in the flow temperature at different locations along the domain were compared to those predicted using direct numerical simulation (DNS) by Christodoulou et al. [54], as seen in Fig. 3b. Further, at a Re of 3900, the simulated Drag Coefficient, C_d, was compared with the experimental data given by Yogini Patel [55]. The numerical drag coefficient from the single-cylinder air model was 0.9105, while Patel [54] found it to be 0.93 ± 0.005, revealing an error of 2.1%.

The comparison of the single-cylinder water model against the Churchill and Bernstein [51] correlation and the experimental data given by Stephen Whitaker [55] can be seen in Fig. 3c and d,

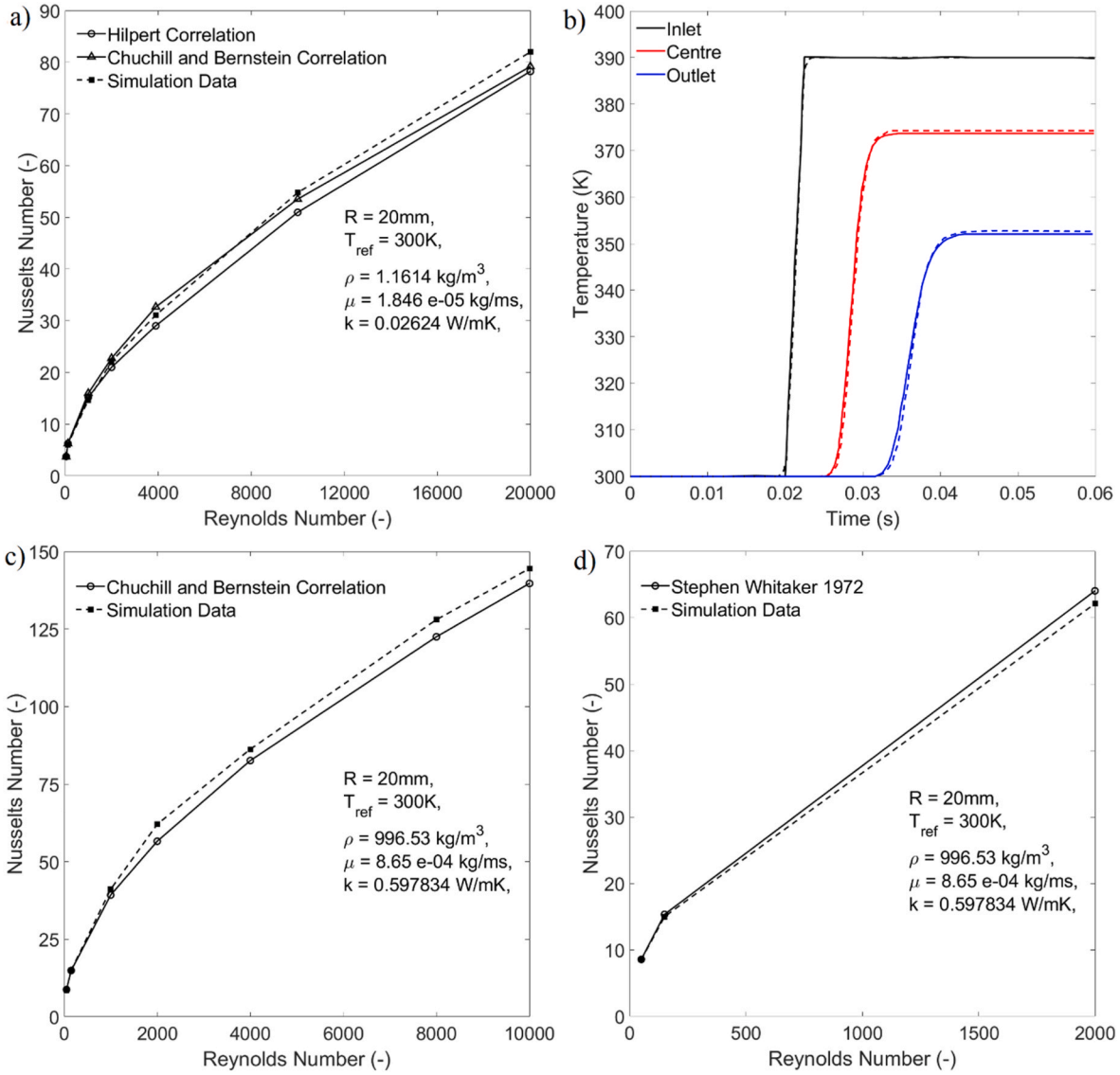

Fig. 3. Comparison of Nusselt number for single cylinder a) air model and Refs. [52,53], b) Comparison of temporal variations in temperature at the inlet, centre and outlet for unsteady response, Re = 180, where the solid-lines and dashed-lines represent DNS and the current simulation, respectively. c) Water model vs numerical data [52] and d) Water model vs experimental data [56].

respectively. As expected, in the laminar regime, both the numerical and experimental data are in excellent agreement with the simulated data. Much like the single cylinder air model, as the value of Re increases, the error also increases. For the comparison against correlation shown in Fig. 3c, the most significant error is 7.89% for Re of 8000, with the minimum error being 0.74% at the Re of 150. Further, for all values of Re, the error is below 4% for the experimental data. Finally, airflow across a bundle of cylinders was also compared against the correlation provided by Grimson [56]. At a Reynolds number of 20,000, the Nusselt number of the model shown in Fig. 1b was found to be 141.72, whereas the Nusselt number calculated using the Grimson correlation was 130.06, leading to an error of 8.97%. The positive agreements among the simulated data, correlations, experimental data, and DNS data for both fluids confirm the validity of the numerical analysis in the present study.

3. Results and discussion

In this section, the battery cells' response to modulations in the volumetric internal heat generation by linear ramps and single cycle segments (see chapter 2) is investigated. It should be noted that since the inlet flow velocity is kept constant, the Reynolds number is kept constant. In forced convection of heat in single phase flows, Nusselt number is primarily a function of Reynolds number and Prandtl number [57], while in battery cooling, the variations in Prandtl number of the coolant are usually insignificant. Therefore, as long as the coolant flow rate and thus Reynold number is kept constant, imposing a ramp in the internal heat generation would result in minor changes to the Nusselt number and the rate of convective cooling. Therefore, the Nusselt number is not visualised during the current analysis; instead, the average surface temperature of the battery cell is considered. This allows for a comparison between the effects of different coolants and the drive cycles, and whether the battery cell's temperature remains within the optimal range. The transient thermal response of the battery module is characterised by calculating the settling time of the average battery temperature and the maximum overshoot. Here, definitions used in the classical theory of system dynamics are employed. Tay et al. [58] describe settling time as the time needed for a system to reach and stay within a percentage range of 2% of the final value, while Ogata [59] defines the maximum overshoot as the peak value of the system response compared to the desired response of the system.

Fig. 4 shows the spatiotemporal response of the coolant's temperature field to a linear ramp in the internal heat generation within each battery cell. This figure corresponds to the ramp in the SC03 drive cycle shown in Fig. 2b. Fig. 4a shows the temperature field in steady-state conditions before introducing the ramp. It should be noted that the simulation was allowed to run for 15 s under steady-state conditions before introducing the ramp – this can be seen in the figures showing the average surface temperature of the battery cell. The fluid and temperature differences between the battery cells become nearly indistinguishable due to the small internal heat generation. However, as the simulation time reaches 50 s, the temperature difference between the battery cell and the fluid can be seen in Fig. 4b. Further, Fig. 4c and d shows the temperature field after 100 s and the end of the simulation, once the system has reached its new steady-state condition. A conventional convective system is shown in Fig. 4; as the fluid flows further downstream, the fluid temperature reaches that of the battery cells. This can be seen clearly in both Fig. 4c and d, cells closer to the inlet exhibit lower temperatures than those at the outlet.

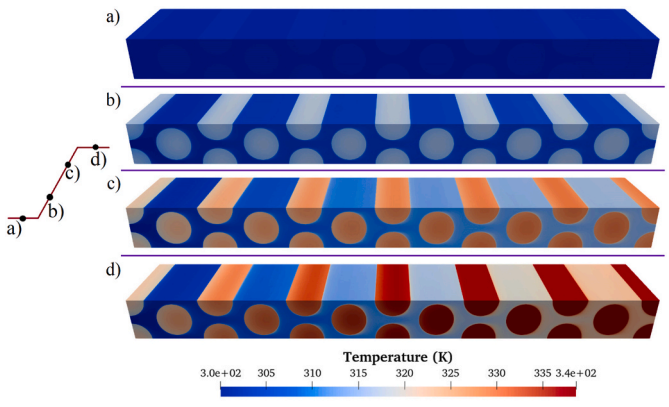

Fig. 4. Temperature field spatiotemporals due to a linear ramp using SC03 driving cycle with the coolant fluid being water. Different stages of the temperature fields a) 15 s – prior to ramp starting, b) 50 s, c) 100 s and d) final steady state condition.

Fig. 5a, c, and e depict the transient response of the average surface temperatures of battery cell to an internal heat generation ramp based on the NYCC1, SC03 and UDDS1 drive cycle with air as the coolant, respectively. Using the speed-time data from Fig. 2a, the NYCC1 ramp was calculated to have a lower limit of 2000 W/m^3 and an upper limit of 47,400 W/m^3 with a duration of 5 s. It can be clearly seen that the temperature of each battery cell continues to rise even after the ramp has finished due to the time taken for the heat to reach the battery surface. Further, each battery cell's overall temperature increase differs from before the ramp until reaching the new steady-state condition. This can be attributed to the behaviour of a typical convective system. As the fluid flows further downstream, it begins to reach the temperature of the battery cells surface, diminishing the convective heat transfer and increasing the time needed to cool down the batteries. This behaviour can also explain the increase in settling time of Fig. 5a as the fluid travels further downstream. A detailed analysis of settling, heating and cooling time for each battery cell will be given later.

Furthermore, a much larger and steeper ramp is found using the speed-time data for the SC03 drive cycle – achieving an upper ramp limit of 196,750 W/m^3 with a total ramp duration of 14 s. The internal heat generation in the SC03 ramp is amplified by over four times compared to NYCC1 in less than three times the duration generating a far steeper ramp and leading to drastically higher battery cell temperatures (see Fig. 5c). As expected with any convective cooling system, as the fluid travels further downstream, the battery cells at the outlet experience higher temperatures than those at the inlet. Although the general trend of temperature increase is similar to those shown in Fig. 5a, due to the significant increase in internal heat generation, the average surface temperature of each battery cell also rises significantly. Comparing the temperature differences between the two drive cycles leads to no obvious correlation. This is to say that increasing the upper ramp limit by four times does not immediately mean that the temperature rise would also be of the same ratio. The trend of an increasing settling time for battery cells further downstream with the NYCC1 data can also be seen in the SC03 data. However, a longer settling time is needed due to a significantly larger internal heat generation.

The UDDS1 ramp leads to an almost identical temperature plot as the NYCC1. This is due to the upper limit of the UDDS1 ramp being 51,700 W/m^3. However, the ramp duration is increased by over two times to 11 s compared to NYCC1. The more significant internal heat generation leads to higher overall temperature increases and more prominent peaks; however, the settling time is shorter than that shown for the NYCC1 case due to the longer ramp duration. This shows that a longer ramp duration for the same upper and lower ramp limits can lead to the system reacting faster to achieve stability, which can be due to the thermal system accommodating the heat release with an increasing internal heat generation. Conversely, cases with a significantly large heat release in a short period would cause a sharp rise in the average surface temperature, resulting in a more considerable time needed to reach steady-state conditions, matching the behaviour shown in Fig. 5a, c and e.

The temporal response of the NYCC1, SC03, and UDDS1 drive cycles to ramps of internal heat generation on each battery cell with water as

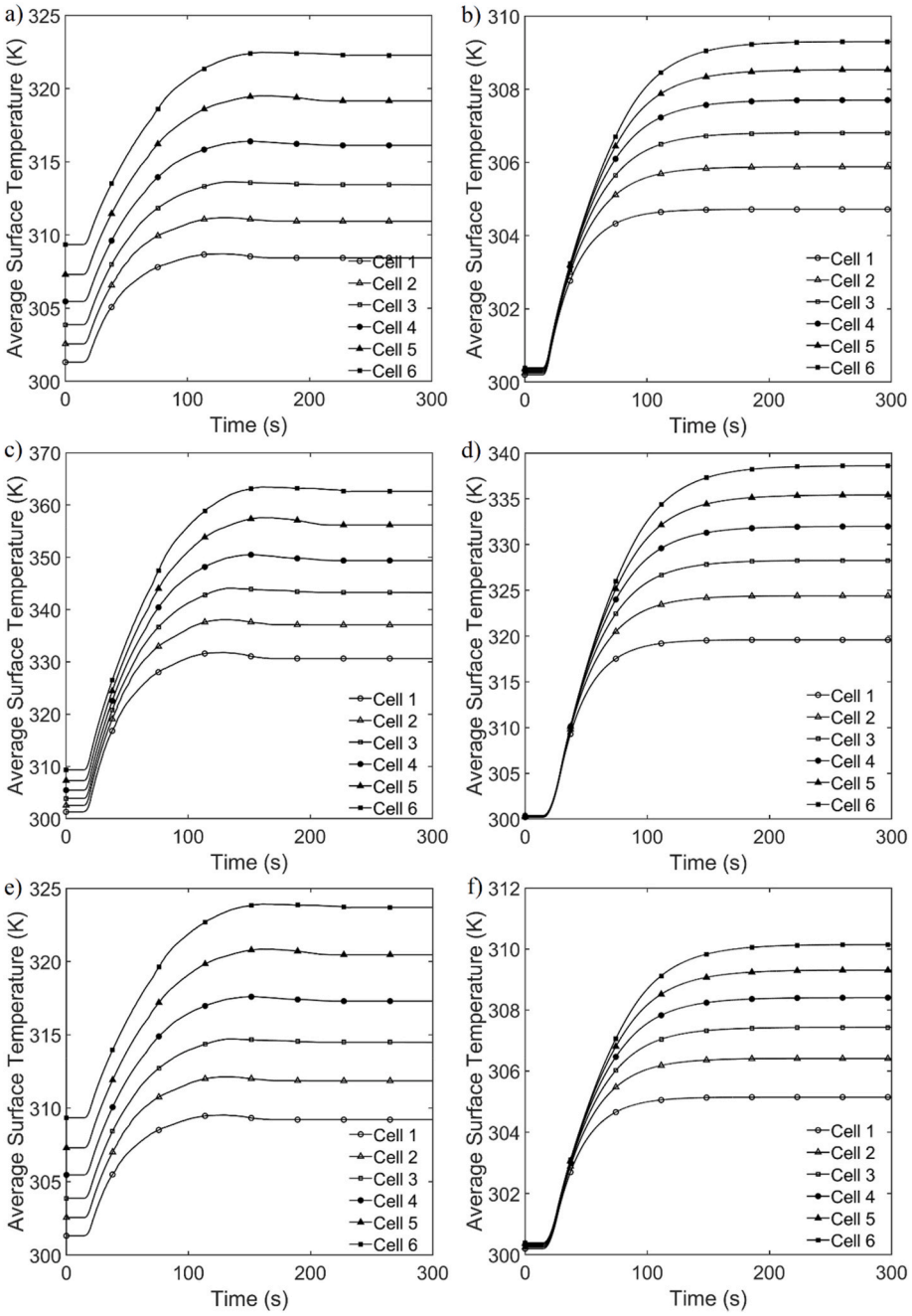

Fig. 5. Average battery cell surface temperature due to internal heat generation ramp with air (left) and water (right) as the coolant fluids using the a) and b) NYCC1, c) and d) SC03 and e) and f) UDDS1 drive cycle data.

the coolant can be seen in Fig. 5b, d and f, respectively. The observed differences between the average surface temperatures for air and water cooling are because the two fluids are significantly different in their thermophysical properties. Unlike the air temperature responses, the water temperature figures show no signs of overshoot. This can be explained by the significant difference in the specific heat capacity of air and water, allowing water to remain at lower temperatures and effectively remove large quantities of heat from the surface of each battery cell. This also explains the significantly lower and tighter starting battery cell temperatures for Fig. 5b, d and 5f.

As expected, in the two responses shown in Fig. 5a and b, where the NYCC1 drive cycle is used, water as the coolant is far more effective at achieving low temperatures. This means that water as the inlet coolant would result in the hottest battery cell being over 30% cooler without over-correction due to overshooting and reaching this state 25.7% faster than air. Furthermore, the recommended operating temperature for a battery ranges from 298 K to 318 K [7], and the cell to cell temperature difference should not exceed 5 K [11]. The case of NYCC1 with water as the coolant achieves all of these conditions. Whereas, for the same case with air, the maximum temperature and cell to cell temperature fall well outside the safe operating range. However, changing the ramp conditions to SC03 with the coolant fluid being water results in very high temperatures falling outside the safe operating range. These temperatures can be seen in Fig. 5d. A decrease of 33.8% for cell one and 28.2% for cell six can be observed compared to the same case with air as the inlet fluid. Further, changing the case from NYCC1 to SC03 increases the settling time due to the increase in internal heat generation.

Fig. 6 shows the values of the dimensionless settling time calculated

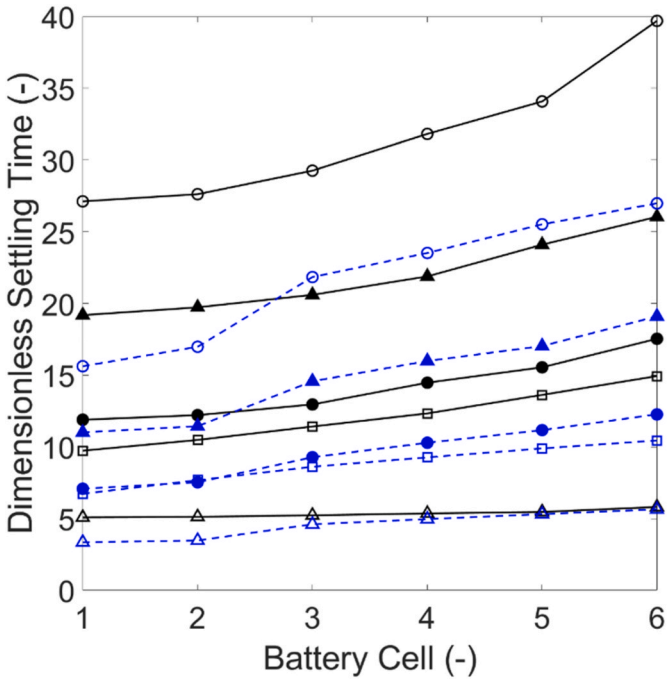

Fig. 6. Dimensionless Settling time for air (black) and water (blue) for each battery cell using different drive cycles: NYCC1 (○), NYCC2 (Δ), SC03 (□), UDDS1 (●), and UDDS2 (▲). (For interpretation of the references to colour in this figure legend, the reader is referred to the Web version of this article.)

of all six primary cells. The dimensionless settling time is defined as

$$\textit{dimensionless settling time}\ (\textit{DST}) = \frac{\textit{settling time}}{\textit{ramp time}} \tag{7}$$

where settling time is the time taken to reach 2% of the final value and the ramp time is the ramp duration. Fig. 6 shows that the DST for downstream cells is always higher than those near the inlet. This behaviour is expected with any regular convective system since the fluid heats up as it moves downstream, necessitating a longer time needed to extract the heat from these cells. Further, numerical simulations wherein air was used always produced a higher DST than those with water as the coolant. The air simulations seem to have a general increase in DST, whereas the water simulation DST jumps from cell 2 to cell 3 before having a general increase in DST on the following cells. Fig. 6 shows that the response of all cells to high ramp duration produces lower values of DST. However, response to shorter ramp periods tends to produce results with a high value of dimensionless settling time. The physical origin of the delay in response to heating in the present problem is heat conduction due to internal heat generation inside the solid battery cells. It is accepted that conduction is the slowest form of heat transfer compared to other forms of heat transfer [57]. The results shown in Fig. 6 indicate that short ramp durations, such as the NYCC1 ramp, release significant amounts of heat within the system very quickly, not allowing enough time for the heat to be conducted from the body of the battery cells to the surface effectively and, as a result, produce high values of DST. Conversely, ramps with a long duration, such as the NYCC2 ramp, have sufficient time to conduct heat from the battery cells to the surface before convection, generating a lower value of DST. This implies that, in practice, changes in the battery cells' internal heat generation over long periods will allow enough time for the heat to be conducted to the surface, allowing the system to react to these changes far quicker. However, short-term disturbances will cause the system to take longer to stabilise.

Furthermore, Fig. 7a and b shows the comparison of the maximum battery cell temperature against the dimensionless settling time and dimensionless heating time, respectively, where the latter is defined as,

$$\textit{dimensionless heating time}\ (\textit{DHT}) = \frac{\textit{time taken to reach}\ \max\ \textit{temperature}}{\textit{ramp time}} \tag{8}$$

It should be noted that since the water simulations produce no overshoot, these simulations tend to take longer to reach the maximum temperature as compared to the air simulations, as shown in the average surface temperature graphs. The use of air as the coolant fluid would produce higher maximum temperatures due to its inferior thermophysical properties than water, which is also why there is a far higher spread between each cell. As discussed in Fig. 6, air-cooling simulations take far longer than water-cooling simulations to stabilise where they can be considered settled; therefore, their dimensionless settling time is also higher. A clear observation from Fig. 7b is that the air simulations produce almost vertically rising results. In contrast, the water simulation results are far more horizontally expanding. This can be explained by the difference in thermophysical properties of each fluid as they continue to impact the degree of DST or DHT reported. Due to air having lower thermal capacity and conductivity, each battery cell would rise to its maximum temperature far quicker, producing an almost vertical line of the maximum cell temperature per drive cycle. However, the large specific heat capacity of water would allow water to retain more heat energy before a temperature rise can be observed. Since the water simulations produce no overshoot, they take longer to reach the

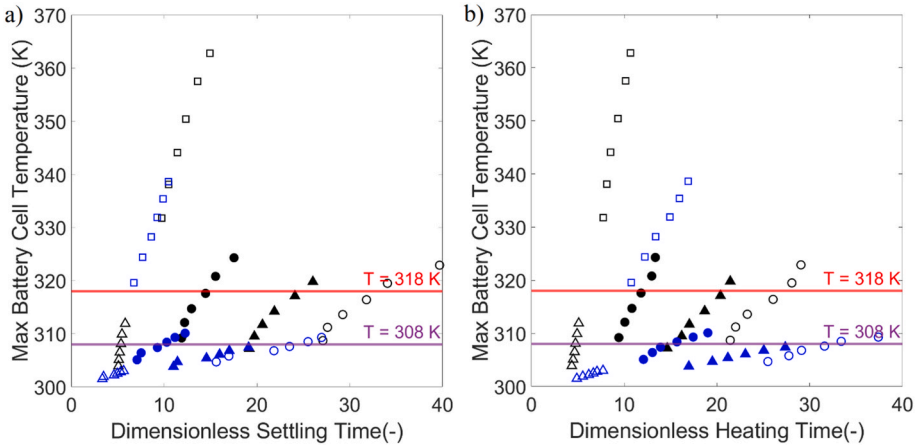

Fig. 7. a) Dimensionless Settling time, and b) Dimensionless heating time, for air (black) and water (blue) for each battery cell using different drive cycles: NYCC1 (○), NYCC2 (Δ), SC03 (□), UDDS1 (●), and UDDS2 (▲). (For interpretation of the references to colour in this figure legend, the reader is referred to the Web version of this article.)

maximum cell temperature. Therefore, the water simulations produce a primarily horizontal trend line for the battery cells per drive cycle, with the only exception being the SC03 drive cycle due to its significantly large internal heat generation. Additionally, two horizontal temperature lines are used to infer if the cells remain within the safe operating range or not. The maximum safe operating temperature of lithium-ion batteries is between 308 and 318 K [11]. Therefore, it can be safely stated that battery cells below 308 K will always remain safe – such as most of the water cooling results. Battery cells between 308 K and 318 K can be considered safe – such as the first four cells in the simulations with the coolant fluid being air using the NYCC1, UDDS1 and UDDS2. However, any battery cells above 318 K will always be out with the safe operating range, which can be observed for both cases of the SC03 drive cycle.

Fig. 8a and b depict the temporal response of the average surface temperatures of battery cells to internal heat generation ramps using the single-cycle segment from the SC03 drive cycle. It can be seen that once the 40-s segment period has finished, the cell surface temperatures continue to rise, reaching a peak before decreasing and reaching a temperature similar to that at the beginning. The steady-state conditions for Fig. 8a and b were set so that if the change in temperature over 10 s was less than 1%, the temperature could be considered stable, and the simulation would stop. Therefore, even though the final temperatures are not the same as the starting temperatures, they are considered stable. Water as the coolant fluid is far quicker at reacting to the changes in the internal heat generation and, as a result, the peak of each cell occurs far quicker and at a lower temperature. The temperature change for cells 1 and 6 where air is the coolant fluid is 22.58 K and 31.33 K, whereas for water cells 1 and 6 change by 15.27 K and 21.49 K. As a result, water can maintain an overall cooler temperature for the battery cells; in particular, the overall temperature increase for cells 1 and 6 is 32.3% and 31.5% lower than air, respectively. Further, the superior thermophysical properties of water than air allow it to react 34% faster for cell 1 and 9.8% faster for cell 6.

Furthermore, Fig. 8c and d shows the maximum battery cell temperature against the dimensionless heating and cooling time. The dimensionless cooling time (DCT) can be defined as the ratio of the time that the battery cell takes to reach a steady state after reaching the peak temperature. As expected, the water results show a far tighter spread of the maximum battery cell temperature than air and show a more horizontal trend line. In particular, in both figures, the case with the NYCC single-cycle segment and water as the coolant fluid produces a horizontal trend line. This is due to the slight increase in internal heat generation over a long period allowing the system to accommodate any changes to the surface temperature. Moreover, it can be clearly seen in Fig. 8a and b that the heating phase of the segment is far smaller than the cooling phase, which can be attributed to the delay in response of the system to changes in the internal heat generation. As the heating phase of the drive cycle segment ends and the cooling phase begins, the surface temperature of the battery cells continues to increase until all the excess heat is removed. This causes the DHT to have a scale from 0.6 to 1.1, whereas the DCT axes range from 2 to 6. Further, as shown in Fig. 7, two horizontal lines are shown in Fig. 8c and d to show the battery cells outside the safe operating range. As expected, using the SC03 single-cycle segment data where water is the coolant fluid, all battery cells remain out of the safe operating range apart from cells 1 and 2. Due to the minor increase in the internal heat generation using the NYCC single-cycle segment, all battery cells continue to reside within the safe operating temperature range.

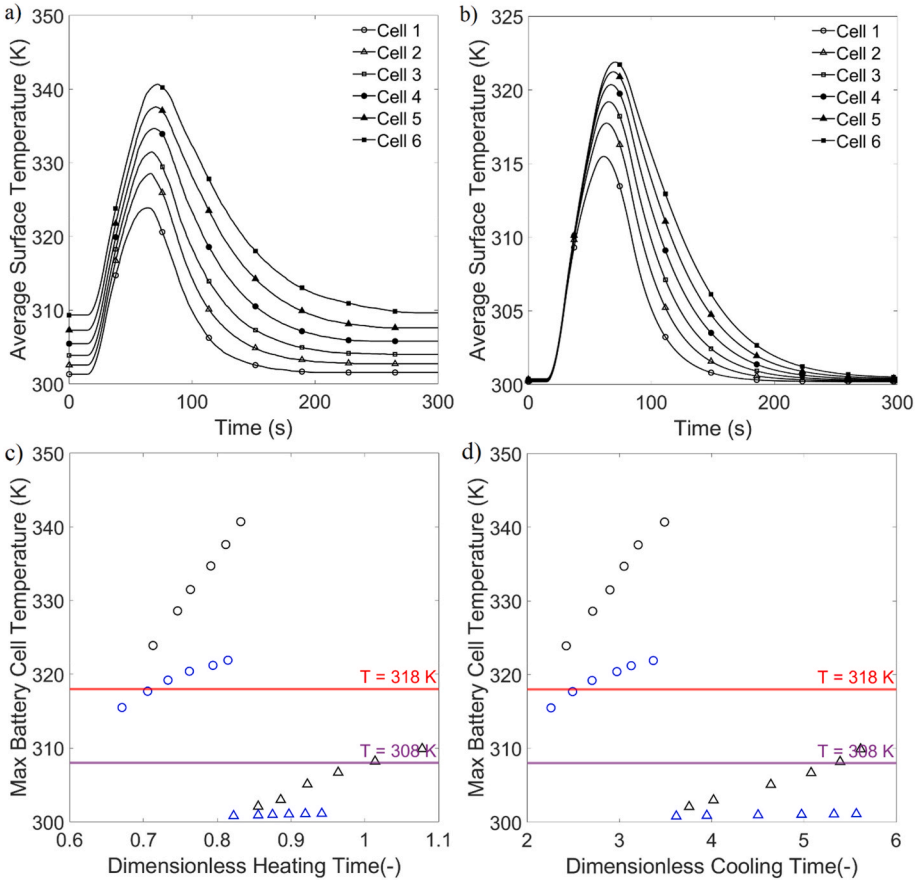

Fig. 8. Average battery cell surface temperature due to SC03 single segment internal heat generation ramp with a) air, and b) water, as the coolant fluids. c) Dimensionless Heating time, and d) Cooling time, for air (black) and water (blue) for each battery cell using different drive cycles: NYCC single segment (Δ) and SC03 single segment (○). (For interpretation of the references to colour in this figure legend, the reader is referred to the Web version of this article.)

4. Conclusions

The battery temperature is impacted by a range of temporal scenarios due to a wide array of driving patterns and vehicle manoeuvres. Therefore, thermal management of battery cells requires predicting their temperature during different driving scenarios. Such predictions are conventional for simple systems with constant parameters. However, they become significantly more complicated when real-time driving data are utilised to predict the state of each battery cell and the battery pack. In this work, three different drive cycles were analysed numerically, using OpenFOAM, to find the points at which the battery cells experience extreme thermal load, such as a very high acceleration in a short period. The system responses were examined by analysing the response of the average surface temperature of each battery cell to linear ramps and single-cycle segments imposed on the internal heat generation. The simulation results for different coolants were then compared in the time domain. The key findings of this study are summarised as follows.

- An imposed ramp on the internal heat generation for cases with air as the coolant fluid always produced a delayed system response and was far slower at reaching the new steady-state condition. However, employing the same ramp for the cases with water as the coolant fluid produced smaller values of DST. This makes it essential to analyse the battery cell response for monitoring the transient thermal response of each battery cell.
- The ramp duration affects the dimensionless settling time. Cases with a large gradient in the ramp, such as NYCC1 (2000 W/m^3 to 47,400 W/m^3 in 5 s), produce high values of DST and create a sharper rise in DST per battery cell.
- For most cases, the use of water as the coolant fluid resulted in the battery cells remaining within the safe operating range.
- Water simulations produced temperature traces with a horizontal line trend. In contrast, air cases tend to produce the results prominently showing a vertical trend line for the maximum battery cell temperature. Additionally, the fluid properties of water allow it to maintain a much tighter spread of maximum cell temperature, reducing the cell-to-cell temperature difference.
- The water single-cycle segment cases react as much as 34% to temporal changes in the internal heat generation during both the heating and cooling phases.

It is evident from the outcomes of this study that battery cooling system might feature transient dynamics that cannot be reconstructed by a series of steady-state tests/simulations. Hence, transient analysis should be an important part of the evaluation of any battery thermal management.

CRediT authorship contribution statement

Ali Saeed: Conceptualization, Software, Validation, Formal analysis, Writing – original draft. **Nader Karimi:** Conceptualization, Supervision, Writing – review & editing. **Manosh C. Paul:** Supervision, Writing – review & editing.

Declaration of competing interest

The authors declare that they have no known competing financial interests or personal relationships that could have appeared to influence the work reported in this paper.

Data availability

Data will be made available on request.

Acknowledgements

Ali Saeed acknowledges the financial support through EPSRC funding (EP/R513222/1) from the University of Glasgow.

N. Karimi acknowledges the financial support by the Engineering and Physical Science Research Council, UK; through the grant number EP/V036777/1.

References

[1] G. Xia, L. Cao, G. Bi, A review on battery thermal management in electric vehicle application, Elsevier B.V, J. Power Sources 367 (Nov. 01, 2017) 90–105, https://doi.org/10.1016/j.jpowsour.2017.09.046.

[2] M. Van Der Steen, R.M. Van Schelven, R. Kotter, M. Van Twist, P. Van Deventer Mpa, EV policy compared: an international comparison of governments' policy strategy towards E-mobility, Green Energy Technol 203 (2015) 27–53, https://doi.org/10.1007/978-3-319-13194-8_2.

[3] S.M. Lukic, J. Cao, R.C. Bansal, F. Rodriguez, A. Emadi, Energy storage systems for automotive applications, IEEE Trans. Ind. Electron. 55 (6) (2008) 2258–2267, https://doi.org/10.1109/TIE.2008.918390.

[4] H. Budde-Meiwes, et al., A review of current automotive battery technology and future prospects, Proc. Inst. Mech. Eng. - Part D J. Automob. Eng. 227 (5) (May 2013) 761–776, https://doi.org/10.1177/0954407013485567.

[5] T.H. Kim, J.S. Park, S.K. Chang, S. Choi, J.H. Ryu, H.K. Song, The current move of lithium ion batteries towards the next phase, John Wiley & Sons, Ltd, Adv. Energy Mater. 2 (7) (Jul. 01, 2012) 860–872, https://doi.org/10.1002/aenm.201200028.

[6] S.M.A.S. Bukhari, J. Maqsood, M.Q. Baig, S. Ashraf, T.A. Khan, Comparison of characteristics-lead acid, nickel based, lead crystal and lithium based batteries, in: Proceedings - UKSim-AMSS 17th International Conference on Computer Modelling and Simulation, UKSim 2015, Sep. 2016, pp. 444–450, https://doi.org/10.1109/UKSim.2015.69.

[7] I.S. Suh, H. Cho, M. Lee, Feasibility study on thermoelectric device to energy storage system of an electric vehicle, Energy 76 (Nov. 2014) 436–444, https://doi.org/10.1016/J.ENERGY.2014.08.040.

[8] H. Kim, S.G. Park, B. Jung, J. Hwang, W. Kim, New device architecture of a thermoelectric energy conversion for recovering low-quality heat, 2013 1144, Appl. Phys. A 114 (4) (Aug. 2013) 1201–1208, https://doi.org/10.1007/S00339-013-7844-7.

[9] S. Arora, Selection of thermal management system for modular battery packs of electric vehicles: a review of existing and emerging technologies, J. Power Sources 400 (Oct. 2018) 621–640, https://doi.org/10.1016/J.JPOWSOUR.2018.08.020.

[10] G. Zhao, X. Wang, M. Negnevitsky, H. Zhang, A review of air-cooling battery thermal management systems for electric and hybrid electric vehicles, J. Power Sources 501 (Jul. 2021), 230001, https://doi.org/10.1016/J.JPOWSOUR.2021.230001.

[11] A.A. Pesaran, Battery thermal models for hybrid vehicle simulations, 2, in: Journal of Power Sources, vol. 110, Aug. 2002, pp. 377–382, https://doi.org/10.1016/S0378-7753(02)00200-8.

[12] C. Zhu, X. Li, L. Song, L. Xiang, Development of a theoretically based thermal model for lithium ion battery pack, J. Power Sources 223 (Feb. 2013) 155–164, https://doi.org/10.1016/J.JPOWSOUR.2012.09.035.

[13] C. Lin, S. Xu, G. Chang, J. Liu, Experiment and simulation of a LiFePO4 battery pack with a passive thermal management system using composite phase change material and graphite sheets, J. Power Sources 275 (Feb. 2015) 742–749, https://doi.org/10.1016/J.JPOWSOUR.2014.11.068.

[14] K. An, P. Barai, K. Smith, P.P. Mukherjee, Probing the thermal implications in mechanical degradation of lithium-ion battery electrodes, J. Electrochem. Soc. 161 (6) (May 2014) A1058–A1070, https://doi.org/10.1149/2.069406jes.

[15] J. Zhang, X. Wu, K. Chen, D. Zhou, M. Song, Experimental and numerical studies on an efficient transient heat transfer model for air-cooled battery thermal management systems, J. Power Sources 490 (Apr. 2021), 229539, https://doi.org/10.1016/J.JPOWSOUR.2021.229539.

[16] C. Roe, et al., Immersion cooling for lithium-ion batteries – a review, J. Power Sources 525 (Mar. 2022), 231094, https://doi.org/10.1016/J.JPOWSOUR.2022.231094.

[17] H. Wang, F. He, L. Ma, Experimental and modeling study of controller-based thermal management of battery modules under dynamic loads, Int. J. Heat Mass Tran. 103 (Dec. 2016) 154–164, https://doi.org/10.1016/j.ijheatmasstransfer.2016.07.041.

[18] R. Zhao, S. Zhang, J. Liu, J. Gu, A review of thermal performance improving methods of lithium ion battery: electrode modification and thermal management system, Elsevier, J. Power Sources 299 (Dec. 20, 2015) 557–577, https://doi.org/10.1016/j.jpowsour.2015.09.001.

[19] M.Y. Ramandi, I. Dincer, G.F. Naterer, Heat transfer and thermal management of electric vehicle batteries with phase change materials, 2011 477, Heat Mass Tran. 47 (7) (Feb. 2011) 777–788, https://doi.org/10.1007/S00231-011-0766-Z.

[20] X. Li, F. He, L. Ma, Thermal management of cylindrical batteries investigated using wind tunnel testing and computational fluid dynamics simulation, J. Power Sources 238 (Sep. 2013) 395–402, https://doi.org/10.1016/j.jpowsour.2013.04.073.

[21] N. Yang, X. Zhang, G. Li, D. Hua, Assessment of the forced air-cooling performance for cylindrical lithium-ion battery packs: a comparative analysis between aligned

and staggered cell arrangements, Appl. Therm. Eng. 80 (Apr. 2015) 55–65, https://doi.org/10.1016/j.applthermaleng.2015.01.049.
[22] L. Yiding, W. Wenwei, L. Cheng, Y. Xiaoguang, Z. Fenghao, A safety performance estimation model of lithium-ion batteries for electric vehicles under dynamic compression, Energy 215 (Oct. 2020), 119050, https://doi.org/10.1016/j.energy.2020.119050.
[23] Z. Ling, F. Wang, X. Fang, X. Gao, Z. Zhang, A hybrid thermal management system for lithium ion batteries combining phase change materials with forced-air cooling, Appl. Energy 148 (Jun. 2015) 403–409, https://doi.org/10.1016/j.apenergy.2015.03.080.
[24] M.J. Sanjari, H. Karami, Optimal control strategy of battery-integrated energy system considering load demand uncertainty, Energy 210 (Nov. 2020), 118525, https://doi.org/10.1016/j.energy.2020.118525.
[25] Y. Huang, S. Wang, Y. Lu, R. Huang, X. Yu, Study on a liquid cooled battery thermal management system pertaining to the transient regime, Appl. Therm. Eng. 180 (Nov. 2020), 115793, https://doi.org/10.1016/J.APPLTHERMALENG.2020.115793.
[26] Y. Fang, J. Shen, Y. Zhu, F. Ye, K. Li, L. Su, Investigation on the transient thermal performance of a mini-channel cold plate for battery thermal management, 303, J. Therm. Sci. 30 (3) (2020) 914–925, https://doi.org/10.1007/S11630-020-1280-8. Aug. 2020.
[27] A. Saeed, N. Karimi, M.C. Paul, Analysis of the unsteady thermal response of a Li-ion battery pack to dynamic loads, Energy 231 (Sep. 2021), 120947, https://doi.org/10.1016/J.ENERGY.2021.120947.
[28] Y. Zhu, Y. Fang, L. Su, F. Ye, Experimental investigation of start-up and transient thermal performance of pumped two-phase battery thermal management system, Int. J. Energy Res. 44 (14) (Nov. 2020) 11372–11384, https://doi.org/10.1002/ER.5757.
[29] J. Kim, J. Oh, H. Lee, Review on battery thermal management system for electric vehicles, Elsevier Ltd, Appl. Therm. Eng. 149 (Feb. 25, 2019) 192–212, https://doi.org/10.1016/j.applthermaleng.2018.12.020.
[30] R. Mahamud, C. Park, Reciprocating air flow for Li-ion battery thermal management to improve temperature uniformity, J. Power Sources 196 (13) (Jul. 2011) 5685–5696, https://doi.org/10.1016/j.jpowsour.2011.02.076.
[31] X.W. Tao, J. Wagner, ASME 2014 Dyn. Syst. Control Conf. DSCC 2014, Cooling Air Temperature and Mass Flow Rate Control for Hybrid Electric Vehicle Battery Thermal Management, vol. 2, Dec. 2014, https://doi.org/10.1115/DSCC2014-6001.
[32] S.J. Drake, et al., Heat generation rate measurement in a Li-ion cell at large C-rates through temperature and heat flux measurements, J. Power Sources 285 (Jul. 2015) 266–273, https://doi.org/10.1016/j.jpowsour.2015.03.008.
[33] W. Wu, X. Xiao, X. Huang, The effect of battery design parameters on heat generation and utilization in a Li-ion cell, Electrochim. Acta 83 (Nov. 2012) 227–240, https://doi.org/10.1016/J.ELECTACTA.2012.07.081.
[34] V.G. Choudhari, D.A.S. Dhoble, T.M. Sathe, A review on effect of heat generation and various thermal management systems for lithium ion battery used for electric vehicle, J. Energy Storage 32 (Dec. 2020), 101729, https://doi.org/10.1016/J.EST.2020.101729.
[35] L.O. Valøen, M.I. Shoesmith, The effect of PHEV and HEV duty cycles on battery and battery pack performance, no. April, Plug-in hybrid Veh. Conf (2007) 1–9 [Online]. Available: https://www.osti.gov/etdeweb/biblio/21007769. (Accessed 12 September 2020).
[36] Tesla Motors Patent US 8286743, Vehicle Battery Pack Ballistic Shield, Dec. 05, 2012 [Online]. Available: http://www.patentlens.net/patentlens/patents.html?patnums=US_8286743. (Accessed 12 September 2020).
[37] X.M. Xu, R. He, Research on the heat dissipation performance of battery pack based on forced air cooling, J. Power Sources 240 (Oct. 2013) 33–41, https://doi.org/10.1016/J.JPOWSOUR.2013.03.004.
[38] J. Zhao, Z. Rao, Y. Li, Thermal performance of mini-channel liquid cooled cylinder based battery thermal management for cylindrical lithium-ion power battery, Energy Convers. Manag. 103 (Oct. 2015) 157–165, https://doi.org/10.1016/J.ENCONMAN.2015.06.056.
[39] C. Lan, J. Xu, Y. Qiao, Y. Ma, Thermal management for high power lithium-ion battery by minichannel aluminum tubes, Appl. Therm. Eng. 101 (May 2016) 284–292, https://doi.org/10.1016/J.APPLTHERMALENG.2016.02.070.
[40] A. Jarrett, I.Y. Kim, Design optimization of electric vehicle battery cooling plates for thermal performance, J. Power Sources 196 (23) (Dec. 2011) 10359–10368, https://doi.org/10.1016/J.JPOWSOUR.2011.06.090.
[41] Ansys FAQ - CFD-Wiki." https://www.cfd-online.com/Wiki/Ansys_FAQ (accessed May 05, 2022).
[42] T.J. Barlow, S. Latham, I.S. Mccrae, P.G. Boulter, A Reference Book of Driving Cycles for Use in the Measurement of Road Vehicle Emissions, Jun. 2009.
[43] V. Muenzel, et al., A comparative testing study of commercial 18650-format lithium-ion battery cells, J. Electrochem. Soc. 162 (8) (May 2015) A1592–A1600, https://doi.org/10.1149/2.0721508JES/XML.
[44] A. Barai, K. Uddin, W.D. Widanage, A. McGordon, P. Jennings, A study of the influence of measurement timescale on internal resistance characterisation methodologies for lithium-ion cells, 81, Sci. Rep. 8 (1) (2017) 1–13, https://doi.org/10.1038/s41598-017-18424-5. Jan. 2018.
[45] J.M. Hooper, J. Marco, G.H. Chouchelamane, C. Lyness, J. Taylor, Vibration durability testing of nickel cobalt aluminum oxide (NCA) lithium-ion 18650 battery cells, Energies 9 (2016) 281, https://doi.org/10.3390/EN9040281, vol. 9, no. 4, p. 281, Apr. 2016.
[46] T. Bruen, J.M. Hooper, J. Marco, M. Gama, G.H. Chouchelamane, Analysis of a battery management system (BMS) control strategy for vibration aged nickel manganese cobalt oxide (NMC) lithium-ion 18650 battery cells, Energies 9 (2016) 255, https://doi.org/10.3390/EN9040255, vol. 9, no. 4, p. 255, Apr. 2016.
[47] Y. Ma, H. Mou, H. Zhao, Cooling optimization strategy for lithium-ion batteries based on triple-step nonlinear method, Energy 201 (Jun. 2020), 117678, https://doi.org/10.1016/j.energy.2020.117678.
[48] T.M. Bandhauer, S. Garimella, T.F. Fuller, A critical review of thermal issues in lithium-ion batteries, J. Electrochem. Soc. 158 (3) (Jan. 2011) R1, https://doi.org/10.1149/1.3515880.
[49] L. Chen, Z. Lü, W. Lin, J. Li, H. Pan, A new state-of-health estimation method for lithium-ion batteries through the intrinsic relationship between ohmic internal resistance and capacity, Measurement 116 (Feb. 2018) 586–595, https://doi.org/10.1016/J.MEASUREMENT.2017.11.016.
[50] D.J. Noelle, M. Wang, A.V. Le, Y. Shi, Y. Qiao, Internal resistance and polarization dynamics of lithium-ion batteries upon internal shorting, Appl. Energy 212 (Feb. 2018) 796–808, https://doi.org/10.1016/J.APENERGY.2017.12.086.
[51] L. Sun, G. Li, F. You, Combined internal resistance and state-of-charge estimation of lithium-ion battery based on extended state observer, Renew. Sustain. Energy Rev. 131 (Oct. 2020), 109994, https://doi.org/10.1016/J.RSER.2020.109994.
[52] S.W. Churchill, M. Bernstein, A correlating equation for forced convection from gases and liquids to a circular cylinder in crossflow, J. Heat Tran. 99 (2) (May 1977) 300–306, https://doi.org/10.1115/1.3450685.
[53] R. Hilpert, Wärmeabgabe von geheizten Drähten und Rohren im Luftstrom, Forsch. auf dem Gebiete des Ingenieurwesens 4 (5) (Sep. 1933) 215–224, https://doi.org/10.1007/BF02719754.
[54] L. Christodoulou, N. Karimi, A. Cammarano, M. Paul, S. Navarro-Martinez, State prediction of an entropy wave advecting through a turbulent channel flow, J. Fluid Mech. 882 (Jan. 2020), https://doi.org/10.1017/JFM.2019.799.
[55] Y. Patel, Numerical Investigation of Flow Past a Circular Cylinder and in a Staggered Tube Bundle Using Various Turbulence Models, Lappeenranta University of Technology, 2010 [Online]. Available: https://lutpub.lut.fi/handle/10024/63863. (Accessed 12 September 2020).
[56] S. Whitaker, Forced convection heat transfer correlations for flow in pipes, past flat plates, single cylinders, single spheres, and for flow in packed beds and tube bundles, AIChE J. 18 (2) (Mar. 1972) 361–371, https://doi.org/10.1002/aic.690180219.
[57] Jack P. Holman, Heat Transfer, tenth ed., McGraw Hill Higher Education, New York, 2010.
[58] T.-T. Tay, I. Mareels, J.B. Moore, High Performance Control, Birkhäuser Boston, Boston, MA, 1998, https://doi.org/10.1007/978-1-4612-1786-2.
[59] K. Ogata, Discrete-time Control Systems, Prentice-Hall, 1987.